SOME ION-BOMBARDMENT EFFECTS ON COPPER-GOLD ALLOYS

by

RICHARD G. NEWCOMBE, B.Sc. (Physics)

PART A: ON-CAMPUS PROJECT*

A Report

Submitted to the School of Graduate Studies

in Partial Fulfilment of the Requirements

for the degree

Master of Engineering

Department of Engineering Physics
McMaster University
Hamilton, Ontario, Canada

August, 1980

*One of two Project Reports: The other part is designated Part B: OFF-CAMPUS PROJECT

MASTER OF ENGINEERING (1980) McMASTER UNIVERSITY

Department of Engineering Physics Hamilton, Ontario

TITLE: Some Ion-Bombardment Effects on Copper-Gold Alloys

AUTHOR: Richard G. Newcombe, B.Sc. (McMaster)

SUPERVISOR: On-Campus : Dr. D.A. Thompson, McMaster

Off-Campus : Professor G. Carter, University of Salford

NUMBER OF PAGES: vii, 41

ACKNOWLEDGEMENTS

I wish to thank my supervisor, Dr. D.A. Thompson[a] for his direction and guidance of the work which led to this report. The members of his research group[a] were also very helpful, especially Dr. S. Poehlman, D. Stevanovic and S. Johar.

Thanks are also due to Professor G. Carter[b] and Dr. J.A. Davies[c] for useful discussions during the course of this work.

(a) Department of Engineering Physics, McMaster University

(b) Department of Electrical Engineering, University of Salford, Salford M5 4WT, Lancashire, U.K.

(c) Solid State Branch, Atomic Energy of Canada, Chalk River, Ontario

ABSTRACT

This report discusses some of the effects of medium-energy ion-bombardment on various copper-gold alloys. Thin (20nm-150nm) films of copper-gold alloys, on Si or SiO_2 substrates, were bombarded with 30keV Ar^+, 45keV Ar^+, or 45 keV Bi^+ ions, to fluences of up to 8×10^{14} ions/mm^2. One of the targets was held at $\sim 50^{\circ}K$; the others were irradiated at room temperature. The effects were observed by 1.00 and 2.00 MeV He^+ ion Rutherford backscattering. The results are discussed in terms of preferential sputtering, gas trapping, and surface topography.

TABLE OF CONTENTS

			Page No.
	Abstract		
Chapter 1:	Introduction		1
Chapter 2:	Theory		
	§2.1:	Preferential Sputtering	2
	§2.2:	Topography Changes	10
	§2.3:	Gas Trapping	11
Chapter 3:	Experimental		
	§3.1:	Sample Preparation	15
	§3.2:	Rutherford Backscattering	16
	§3.3:	Ion Implantation and Rutherford Backscattering Facility	17
	§3.4:	Electrostatic Quadrupole	18
Chapter 4:	Results and Discussion		20
Chapter 5:	Conclusions		29

Tables

Table I : Sputtering Yield Ratios for an Alloy $A_{.5}B_{.5}$: Low Order Recoil Effect; Derived by Kelly[3], equation 8 — 31

Table II: Sputtering Yield Ratios for an Alloy $A_{.5}B_{.5}$: Cascade Effect; Derived by Haff[5], equation 10 — 31

Table III: Sputtering Yield Ratios for an Alloy $A_{.5}B_{.5}$: Surface binding energy Effect; Derived by Kelly[3], equation 18 — 31

Table IV: Theoretical and Experimental Sputtering Yields — 32

Page No.

Figures

Figure 1 : Pickering Model: Steady-State Concentration Profile of Component A 33

Figure 2 : Collins Model: Steady-State Concentration Profile of Component A 33

Figure 3 : Variation of Sputtering Yield with Ion Incidence Angle 34

Figure 4 : Non-Monotonic Collection of Ar in Si 34

Figure 5 : RBS Spectrum of $Cu_{.71}Au_{.29}$ on Si Substrate; 2.0 MeV He^+, $\theta_L = 150°$ 34

Figure 6 : Schematic of McMaster On-Line RBS and Ion-Implantation Facility 35

Figure 7 : Schematic of Electrostatic Quadrupole 36

Figure 8 : Sputtering of $Cu_{.69}Au_{.31}$ by 45 keV Ar^+ 36

Figure 9 : Sputtering of $Cu_{.71}Au_{.29}$ (sample #1) by 45 keV Ar^+ 36

Figure 10: T.E.M. Electron Diffraction Patterns of Cu_3Au 37

a) before ion bombardment
b) after bombardment with 500 eV Ar^+

Figure 11: Sputtering of Cu-Au Alloy Films with 30 and 45 keV Ar^+ 38

Figure 12: 45 keV Ar^+ Collection Curves in Cu-Au Alloy Films

Figure 13: S.E.M. Photographs of $Cu_{.71}Au_{.29}$ (sample #2) 39

a) before ion bombardment
b) after bombardment with 8.3×10^{14} ions/mm^2 of 45 keV Ar^+

Page No.

Figure 14: S.E.M. Photographs of $Cu_{.94}Au_{.06}$ after 6.7×10^{14} ions/mm^2 of 45 keV Ar^+ 39

a) 5,000X magnification
b) 20,000 magnification

References 40

CHAPTER 1

INTRODUCTION

Many materials are used in environments in which they are subjected to particle irradiation. Understanding the effects of this irradiation, particularly on metal alloys, is very important in current fission reactors and potentially important in future fusion reactors. Furthermore, ion beams are commonly used for sputter-cleaning of surfaces, for sputter-machining, and for sputter-profiling when used in conjunction with surface analysis techniques such as Auger-electron spectroscopy and secondary ion mass spectrometry.

Ion bombardment introduces impurities into the target, as well as depositing energy into the target, resulting in ionization, and displacing atoms from their lattice positions. At the surface, ion bombardment will remove atoms (sputtering), and may remove one component of an alloy faster than others (preferential sputtering); or it may remove atoms faster in one location than another, changing the surface topography.

CHAPTER 2

THEORY

§2.1 Preferential Sputtering

An energetic ion incident upon a solid target deposits its energy into ionization and electronic excitation through inelastic collisions, and into atomic displacements through elastic collisions. Atoms displaced within about the first two monolayers at the surface may escape the solid: sputtering.

The number of atoms released per incident ion is the sputtering yield, S. The sputtering yield depends upon the binding energies of the target atoms and the energy deposited into elastic collisions at the surface. This surface deposited energy depends upon the ion energy, the atomic mass and atomic number of both the ion and the target atoms. Sigmund[1] developed a model for sputtering of elemental targets, assuming a planar surface, which fits the available experimental data quite well, as long as the deposited energy density at the surface is less than $\sim$10eV nm^2/atom.[2] Sigmund's[1] model gives the sputtering yield as

$$S = \Delta x \, F_D(0)/\pi^2 U_o \qquad (1)$$

where: U_o is the surface binding energy per atom; $F_D(0)$ is the energy deposited in elastic collisions at the surface; and Δx is the depth over which the deposited energy

contributes to sputtering. Sigmund[1] gave

$$\Delta x \simeq 3/4NC_o \qquad (2)$$

which is approximately the range of an average recoiling atom, of the order of 0.5nm-1.0nm. Here, N is the number density of atoms in the target, and C_o is constant which Sigmund used for a low energy collision cross-section approximation. (See pg. 184, ref. 1)

If the target is an alloy, complications arise, due to: a) the different masses of the target atoms, which affect the collision cross-sections, the recoil ranges, and the energy transferred in collisions; b) different surface binding energies; and c) different vapour pressures.

Kelly[3] showed that mass effects cause the lighter atoms to sputter faster, proportionally, than the heavier atoms. He extended the Kelly-Sanders[4] model of recoil implantation to deal with atoms sputtered from the surface by the action of low-order recoil atoms. He took the target to be an alloy AB, with atomic masses M_A and M_B, and an average atomic mass M_3, in the unsputtered bulk of the target. He let x_A and x_B be the atomic fraction of atoms of A and B, and $j(M_3/M_A)$ and $j(M_3/M_B)$ be functions of the recoil atom distribution:

$$j(M_3/M_A) \simeq (2h)^{\frac{1}{2}} \int dw \cdot w^{-1/3} \cdot \text{ierfc}\{fw/(2h)^{\frac{1}{2}}\}, \qquad (3)$$

where: $(2h)^{\frac{1}{2}} = \frac{\langle y \rangle N_3 C}{T_2^{2/3}} \cdot \sqrt{2}$, (4)

N_3 is the average number density of atoms in the target, C is a constant similar to C_o, $\langle y \rangle$ is the average distance an incident ion is deflected from its initial line of motion (called the "mean projected transverse straggling"), and T_2 is the energy transferred, in a low order recoil, from the incident particle (mass M_1, energy E) to the target particle (mass M_2):

$$T_2 = E \cdot \frac{4M_1M_2}{(M_1 + M_2)^2} \cdot w \quad (5)$$

where $w = \sin^2 (\theta/2)$ (6)

and θ is the centre-of-mass angle between the line of motion of the target particle and the initial line of motion of the incident particle;

$$f = \langle x \rangle N_3 C / T_2^{2/3}, \quad (7)$$

where $\langle x \rangle$ is the mean projected range of the ions in the target.

Kelly then obtained

$$\frac{S_A}{S_B} = \frac{x_A M_B^{1/3} (M_1+M_B)^{2/3}}{x_B M_A^{1/3} (M_1+M_A)^{2/3}} \left(\frac{M_1^{2/3} + M_B^{2/3}}{M_3^{2/3} + M_B^{2/3}} \right)^{2/3} \cdot \left(\frac{M_3^{2/3} + M_A^{2/3}}{M_1^{2/3} + M_A^{2/3}} \right)^{2/3} \cdot \frac{j(M_3/M_A)}{j(M_3/M_B)} \quad (8)$$

Some representative sputtering yield ratios, calculated from equation 8, are given in Table I.

Haff[5] assumed that the energy deposited in a collision cascade becomes evenly distributed among the displaced particles, independent of mass, and then showed that the mean recoil distance is

$$L \simeq (\bar{v}\bar{l}\tau)^{\frac{1}{2}} \tag{9}$$

where $\bar{v}$ is the average recoiling particle's velocity, $\bar{l}$ is the collision mean free path of a recoil in a collision cascade, and τ is the cascade lifetime, approximately the slowing-down time of the incident ion, of the order of 10^{-13} seconds. Then

$$\frac{S_A}{S_B} = \frac{L_A}{L_B} = \left(\frac{M_B}{M_A}\right)^{\frac{1}{4}} \tag{10}$$

with typical results given in Table II.

A second factor which Kelly[3] considered was the sputtering caused by high-order recoil atoms from the bulk of the target knocking off surface atoms. He used the atom flux derived by Winters and Sigmund[6]:

$$P = K_3 \cos\theta / T_3^3 \tag{11}$$

where P is the probability of an atom coming from the bulk with energy T_3, at angle θ to the surface normal, and K_3 is a constant. From Andersen and Sigmund[7] he obtained

$$P_A/P_B = x_A/x_B \tag{12}$$

and then calculated that

$$\frac{S_A}{S_B} = \frac{x_A U_B}{x_B U_A} \cdot \frac{x_A + x_B \gamma}{x_B + x_A \gamma}, \tag{13}$$

where U_A and U_B are the surface bonding energies of A and B atoms and $\gamma = 4M_AM_B/(M_A + M_B)^2$. (14)

This would lead to the target surface becoming depleted in the more abundant component, not necessarily the lighter component.

The third factor Kelly[3] calculated is that due to surface binding energies alone. Taking U_{AA} as the nearest neighbor A-A bond energy, U_{AB} and U_{BB} as similar energies, and Z_s as the coordination number for an atom in the surface monolayer, then

$$U_A = x_A Z_s U_{AA} + x_B Z_s U_{AB} \tag{15}$$

He approximated

$$U_{AA} \simeq \tfrac{1}{2} Z \Delta H_A \tag{16}$$

where Z is the bulk coordination number of pure A, and ΔH_A is its heat of atomization. Similarly, he approximated

$$U_{AB} \simeq \tfrac{1}{4} Z (\Delta H_A + \Delta H_B) \tag{17}$$

From equations 15, 16, and 17 he obtained:

$$\frac{S_A}{S_B} = \frac{x_A}{x_B} \cdot \frac{x_B \Delta H_B + \tfrac{1}{2} x_A (\Delta H_A + \Delta H_B)}{x_A \Delta H_A + \tfrac{1}{2} x_B (\Delta H_A + \Delta H_B)} \tag{18}$$

Some typical results of equation 18 are given in Table III.

Finally Kelly[3] considered the effect of vapour pressures. Any local heating caused by the ion beam, either on the microscopic scale (within the collision cascade) or on the macroscopic scale (heating of the bulk

of the target), will cause the more volatile component to sputter preferentially.

Comparing these calculations to experimental data, Kelly[3] found that his first (low-order recoil) and third (surface binding energy) factors agree qualitatively with observations of the sputtering of metal alloys, but that his second (high-order recoil) factor does not. Furthermore, vapour pressure effects seem to be irrelevant to metal alloys. Haff's[5] results agree qualitatively with Kelly's[3] first factor. Haff[5] showed that they agree quantitatively with the observations of Liau et al[8], for $Au_{.19}Ag$, Cu_3Au, $AuAl_2$, NiSi, Pt_2Si, and Au_2Al.

The change in stoichiometry due to preferential sputtering will result in the composition changing until the target reaches a steady-state, after which it sputters stoichiometrically, ie. such that the ratio of the sputtering yields equals the ratio of atoms in the bulk. This must be so, to conserve mass. For preferential sputtering restricted to the near surface region, this steady state condition will be reached rapidly. However, if atoms can diffuse to or from the surface at an appreciable rate, the region of non-stoichiometry will be extended. Therefore it will take longer to reach a steady-state. If the sputtering rate is low enough, and diffusion is fast enough, the steady-state sputtering may be non-stoichiometric.

One of the first attempts to model preferential

sputtering was by Shimizu et al.[9] Using Auger electron spectroscopy, they probed the top 1.0-2.0nm of small-grain Cu-Ni alloys, before and after irradiation with a 500eV Ar^+ ion beam. They found that the surface was depleted of Cu by the irradiation. To explain this they set up the equation:

$$\frac{dC_{Ni}^{s}}{dt} = \phi\left(-S_{Ni}C_{Ni}^{s} + S_{Ni}C_{Ni}^{s}C_{Ni}^{o} + S_{Cu}C_{Cu}^{s}C_{Cu}^{o}\right) \quad (19)$$

where: C_{Ni}^{s} is the surface concentration of Ni in atomic per cent;

C_{Ni}^{o} is the bulk concentration of Ni in atomic per cent;

S_{Ni} is the sputtering yield of Ni in the alloy;

and similar definitions for S_{Cu}, C_{Cu}^{s}, C_{Cu}^{o}; and ϕ is the flux of Ar^+ ions, in ions/cm^2sec.

The first term of equation 19 gives the rate of removal of Ni atoms; the second term gives the rate of exposure of Ni atoms where Ni atoms have been sputtered off; and the third term gives the rate of exposure of Ni atoms where Cu atoms have been sputtered off. After sufficient irradiation, the surface reaches a steady-state composition, such that

$$dC_{Ni}^{s}/dt = 0 \quad (20)$$

from equations 19 and 20, it can be shown that

$$C_{Ni}^{s}(\text{at steady-state}) = RC_{Ni}^{o}/(1 - C_{Ni}^{o} + RC_{Ni}^{o}) \quad (21)$$

where $C_{Cu}^{o} = 1 - C_{Ni}^{o}$ (22)

and $R = S_{Cu}/S_{Ni}$ (23)

By curve-fitting the experimental results obtained[9] to equation 21, it was found that , at steady-state, R = 1.9 for the whole range of Cu-Ni alloys tested. This violates the conservation of mass, unless diffusion was sufficiently fast that the depleted Cu atoms were continually being replaced by Cu atoms from the bulk.

Pickering[10] started by assuming that, in a binary alloy AB, at steady-state,

$$R = C_A^{\,o}/C_B^{\,o} \quad . \tag{24}$$

In order to simplify the problem, he assumed that, under ion-irradiation, one of the alloy elements (A) would diffuse much faster than the other (B), making A effectively a solute in an eroding solvent lattice. If the A atoms sputter off much faster than the B atoms, then $C_A^{\,s} \simeq 0$. Pickering applied Fick's second law of diffusion:

$$\frac{dC_A(x)}{dt} = D_A \frac{d^2C_A(x)}{dx^2} \tag{25}$$

where D_A is the diffusion coefficient of A in the alloy under irradiation. He assumed that the surface erodes at a constant rate,

$$v = \phi S / N_B \tag{26}$$

where N_B is the number density of B atoms. The surface at any point in time is at

$$x = x_o = vt. \tag{27}$$

This leads to a steady-state solution:

$$N_A(x) = N_A^{\,o}\left[1 - \exp\left(\frac{-v\,[x - x_o]}{D_A}\right)\right] \qquad (28)$$

This is illustrated in Fig. 1.

This model does not seem applicable to metal alloys, because of the assumptions that $D_A \gg D_B$, and $C_A^{\,s} \simeq 0$. However, it may apply to some volatile oxides, in which the oxygen sputters off very much faster than the other element, and also diffuses much faster.

Collins[11] and Webb, Carter and Collins[12] also attempted analytic descriptions of preferential sputtering. Collins[11] assumed $D_A = D_B$ = a constant over the entire depth of a semi-infinite solid. Webb et al.[12] assumed that $D_A \gg D_B$, but also assumed that diffusion is only significant in the region of deposition of energy by the ion. Both models result in profiles like Fig. 2.

§2.2 Topography Changes

Irradiation by heavy ions causes considerable perturbation to the surface of a solid. Much of the ions' energy goes into displacing atoms from their equilibrium positions. The point defects created may diffuse to sinks, or form dislocations or voids. The incident ions, once stopped in the solid, may aggregate to form regions of a different chemical phase; if they are inert gas ions, they may form bubbles in the solid. Any of these perturbations, when exposed to the surface by sputter-removal

of the atoms above them, will alter the shape of the surface.

Furthermore, the sputtering yield is a function of angle: defining the yield at normal incidence as $S(0^{\circ}) = S_o$, then Sigmund's theory[1] gives:

$$S(\theta) = S_o \cdot (\cos \theta)^{-n} \qquad (29)$$

where $n \gtrsim 1$. Experiments[13] show that this only applies to $0^{\circ} \leq \theta \lesssim 65^{\circ}$; at larger angles, the sputtering yield decreases as reflection of the ion beam becomes significant (see Fig. 3). Hence any pits and hollows formed in a surface will tend to be enhanced, since the ion beam will not hit the walls at normal incidence, therefore sputtering them faster.

Small impurities on the surface may sputter slower than the target itself, leading to the formation of mesas. Inclusion impurities exposed to the surface by sputtering will have the same effect. There is also some preferential sputtering due to crystallographic effects[14]: the yield may be higher in some crystalline directions than in others. Hence a polycrystalline surface may tend to develop bumps and hollows, whose dimensions will depend on the grain sizes and misorientations. For more detail, see references 14-17.

§2.3 Rare Gas Trapping[18]

Once an ion has entered a solid, there are two

major factors which determine η, the probability that it will be captured, and remain in the solid. One is the trapping probability, which may be expressed as a cross-section, σ_{tr}-it is the probability that, after an ion has been slowed to thermal velocities, it will fall into a potential well which can immobilize it. The other is the release probability, which may also be expressed as a cross-section, σ_r -it is the probability that the trapped atom will be released from the solid by the direct or indirect action of the ion beam. Of course, there is no reason that there cannot be several trapping and release mechanisms each with an appropriate cross-section. In most cases, theory and experiment agree that there are many mechanisms, although one or two may dominate.

In almost all cases, the net rate of collection of implanted rare gas ions is largest at the beginning of the implantation, and decreases monotonically until a saturation level is reached. This saturation level is generally independent of the ion flux, unless the flux is great enough to heat the target, or small enough that diffusion can alter the effective penetration range of the ions. The larger the penetration range, the more trapping sites are available, and hence the more rare gas atoms can be trapped.

Non-monotonic increases in N_T (the number of rare gas atoms trapped per unit area), such as in Fig. 4,[19] is

thought to be due to two factors. One is the formation and bursting of gas bubbles and blisters. The other is the influence of the trapped gas on the stopping power of the target: this changes the ion range and energy deposition profiles. The former has been discussed above; the latter change may alter the rate of release of already trapped gas atoms, and if it affects $F_D(0)$, will alter the sputtering rate, as well. These factors are inter-related and diffusion dependent.

Therefore, at any point in time, trapping and release of rare gas atoms will depend upon the depth of distribution of already trapped gas. Another factor in the importance of the trapped gas distribution is that gas atoms trapped very near the surface may have a greater probability of escaping from the target, because of the shorter distance they have to travel, and the often sharp concentration gradients near the surface. Also, implanting large quantities of gas may force some of it into less accessible sites, as other sites begin to saturate.

A first approximation[18] to describe the gas collection assumes that the target has a fixed number of trapping sites. Then

$$\frac{dN_t}{d\Phi} = I_0 \sigma_t \left(1 - \frac{N_t}{N_{sat}}\right) \tag{30}$$

where Φ is the ion fluence, and N_{sat} is the saturation number of trapped gas atoms per unit area. This doesn't explain most collection data, because there is release of some of the trapped gas by the action of the incident ions, and because the ions usually create some of their own trapping sites by displacing target atoms, in the process of being stopped.

A second approximation[18] uses one or more trapping cross-sections, σ_1, σ_2,... and one or more release cross-sections, σ_{r1}, σ_{r2}, ... Letting $N_T = N_1 + N_2 + \ldots$ then $dN_T/d\Phi$ is obtained by solving the simultaneous equations:

$$\frac{dN_1}{d\Phi} = \Phi\sigma_1\left[1 - \frac{N_1}{N_{sat_1}}\right] - \sigma_{r1}N_1 \qquad (31)$$

$$\frac{dN_2}{d\Phi} = \Phi\sigma_2\left[1 - \frac{N_2}{N_{sat_2}}\right] - \sigma_{r2}N_2 \qquad (32)$$

The boundary conditions are not easy to determine, especially if there is significant re-trapping of gas atoms released from their traps.

CHAPTER 3

EXPERIMENTAL

§3.1 Sample Preparation

The samples consisted of thin films (20nm to 150nm) of Cu-Au alloy on substrates of polished, cleaned single crystal Si wafers, except in the case of the 99% Au film, which was on a substrate on which 100nm of oxide had been thermally grown, in order to avoid the problem of mixing of the Si and Au which Blank and Wittmaack[20] observed. A low atomic mass substrate was required in order to be able to resolve the Au and Cu signals in the Rutherford backscattering (RBS) analysis.

The films were evaporated onto the substrates in an evaporator system with a base pressure of 5×10^{-6} Pa. Carefully weighed chunks of Cu and Au were placed in a tungsten boat, melted together by an electron beam, and then evaporated. The samples were annealed for ten minutes at 290°C, in a small furnace evacuated to 5×10^{-4} Pa. Care was taken not to raise the film temperatures above the eutectic temperature, 300°C, in order to maintain a uniform solid solution, and avoid the formation of precipitates of CuAu, Cu_3Au, and/or $CuAu_3$. From the RBS spectra it was clear that most of the sample films were uniformly alloyed, with no significant mixing into the substrates. Non-uniform films were discarded.

§3.2 Rutherford Backscattering

The main tool for analysis of surfaces used for this report is Rutherford backscattering. MeV He^+ ions collide with atoms in a way which is described extremely well by the Rutherford model. The collisions are elastic, Coulombic collisions between the He nuclei and the target nuclei. Without the small correction for electronic screening of the nuclear charge in the case of high atomic number target atoms[21], the Rutherford differential scattering cross-section is given by

$$\frac{d\sigma}{d\omega} = 1.296 \times 10^{-25}\left(\frac{Z_1 Z_2}{E_o}\right)^2 \left(\frac{M_1 + M_2}{M_2}\right)^2 \sin^{-4}(\theta_s/2) \qquad (33)$$

where $d\sigma/d\omega$ is the scattering cross-section of incident ions of atomic mass M_1, atomic number A_1, and initial energy E_o, scattered by a target atom of atomic mass M_2, atomic number Z_2, into a unit solid angle at center-of-mass scattering angle θ_s. E_o is in MeV, in order to give $d\sigma/d\omega$ in mm^2/steradian.

The total number of scattered ions detected is

$$Y = (N\Delta x)n\left(\frac{d\sigma}{d\omega}\right)\Delta\omega \qquad (34)$$

where $N\Delta x$ is the areal density of target atoms (atoms/mm^2), n is the fluence of incident ions (ions/mm^2) and $\Delta\omega$ is the solid angle subtended by the detector (steradians).

He^+ ions which are backscattered by the surface monolayer will have an energy dependent on the mass of the

He^+ ion and that of the target atom, according to

$$E_1 = k^2 E_o = \left(\frac{M_1 \cos\theta_L + M_2}{M_1 + M_2} \right)^2 E_o \qquad (35)$$

where, now, θ_L is the scattering angle in <u>laboratory</u> coordinates. Therefore one can identify a target atom by the energy of He^+ ions which scatter from it through a well-defined, known angle. See Fig. 5.

Ions which penetrate beneath the surface will steadily lose energy through electronic excitation and ionization, before and after being backscattered. If the rate of energy loss as a function of energy is known, the energy spectrum of the backscattered ions can be converted to a depth profile of the target atoms. For more detail, see reference 22.

§3.3 Ion Implantation and RBS Facility

The samples were ion implanted and RBS analysed in situ, in the McMaster University Accelerator Lab, Solid State Facility.(See Fig. 6). A 150 kV accelerator provided beams of 30keV Ar^+, 45keV Ar^+, 45keV Bi^+, at fluences of from 10^{13} ions/mm^2. An on-line 3MV Van de Graaf accelerator provided 1-2 MeV He^+ beams, with currents of 2-10 nA.

The ions were mass-energy analysed by passing through a magnet and several defining apertures. The magnet had to bend the He^+ ion beam through 25^o, and the Bi^+

and Ar^+ ions through 40^o. For the Bi^+ and Ar^+ ion implants, the apertures were off-axis, so as to minimize the proportion of ions reaching the target after being neutralized in a charge-exchange collision with gas atoms in the beamline. The beam first passed through a 2mm diameter aperture, then was swept vertically and horizontally across a 4mm aperture, close to the target, to ensure implant uniformity.

In the case of the MeV He^+ beams, charge exchange is negligible. The apertures were both on-axis, and 0.75mm in diameter. The apertures were 0.96m apart to ensure good collimation of the analysing beam.

The MeV He^+ ions were backscattered at 150^o into a surface barrier detector, the output of which was pulse-height analysed to give energy spectra of the backscattered particles.

The target chamber reached pressures of 3×10^{-5} Pa. A copper cylinder surrounding the target was cooled to about 25^oK, reducing the effective pressure at the target surface to about 3×10^{-8} Pa. In one of the experiments, the target was connected to this copper shield, and thereby cooled to $\lesssim 50^oK$.

§3.4 Electrostatic Quadrupole

When the ion beams from the 150 kV accelerator pass through the magnet, they are generally quite broad- as much as 10mm in diameter- and not always circular in

cross-section, since the analysing magnet focuses in the horizontal plane, but not vertically. In order to improve the focus, to get higher ion fluxes at the target, an electrostatic quadrupole lens was built.

The quadrupole, or "stigmator", was composed of four 15 inch electrodes, each a 120^{o} section of a 1 1/8 inch diameter aluminum rod (see Fig. 7) supported at 90^{o} intervals by insulating rings, in a two inch diameter beamline. The beam aperture was then 7/8 inch, or 22mm, in diameter. The electrodes were charged in pairs, with opposite electrodes having the same charge. The focal length, as given by Hawkes[23], is

$$X = 1/\alpha \sin(\alpha L) \tag{36}$$

where $$\alpha = V_1/V_o a^2 \tag{37}$$

and V_1 is the quadrupole voltage, V_o is the ion acceleration voltage, "a" is the beam aperture diameter, and L is the electrode length. With $X \simeq 2.5$m, a = 0.022m, L = 0.38m, and $V_o \sim 50$kV, the electrodes need only be charged up to 10-50V.

CHAPTER 4

RESULTS AND DISCUSSION

Following Kelly's[3] and Haff's[4] reasoning, it was expected that there would be some preferential Cu loss in the sputtering of Cu-Au alloys. Table I, from equation 8, shows that Kelly's[3] low-order recoil factor would predict $S_{Au}/S_{Cu} \simeq 0.31$, for a 50% Cu, 50% Au alloy (M_{Au}/M_{Cu} = 197/63.54 = 3.1). However, Haff[4] would predict $S_{Au}/S_{Cu} \simeq 0.76$, as shown in Table II, from equation 10; and Kelly's[3] surface binding energy effect (Table III, equation 18) would predict $S_{Au}/S_{Cu} \simeq 0.94$. These predictions strictly apply only to a $Cu_{.5}Au_{.5}$ alloy, but the trend to preferentially sputter Cu should apply to all Cu-Au alloys.

No preferential sputtering was observed in this work. This does not necessarily prove that there was no preferential sputtering, since, at a scattering angle of 150°, with a detector resolution of 16keV, the depth resolution of 2.00 MeV He^+ ion RBS is 17nm in $Cu_{.5}Au_{.5}$. Any preferential sputtering which is not diffusion fed, and therefore not extended over greater than a few nanometers, would not be distinguishable by looking at the shapes of the Cu and Au peaks in the RBS spectra, because the effect would be averaged over the 17nm.

Gillam[24] and Liau et al.[8] have observed preferential sputtering in Cu_3Au. On the other hand, Färber et al.[25]

saw no preferential sputtering in Cu_3Au.

Gillam[24] did transmission electron microscopy (TEM) of thin foils of Cu_3Au, before and after bombardment with Ar^+ ions at energies up to 4keV. The TEM patterns before ion bombardment showed a set of Debye-Scherrer rings corresponding to the f.c.c. lattice of Cu_3Au (see Fig. 10a). After bombardment, the TEM pattern showed the formation of a second set of rings inside the first, indicating a layer of material with a larger lattice parameter than Cu_3Au, and therefore enriched in Au. The layer was thought to be essentially uniform, because the rings in the second set were sharp, and distinct from the original rings. The new layer was shown to be a surface layer by the fact that the second set of rings were fainter after the sample had been lightly etched. From the relative intensities of the rings, and from weight and thickness measurements of the foils, it was estimated that the altered layer had a thickness of approximately one ion range. The composition of the layer depended on the Ar^+ ion energy: 21eV ions produced a few monolayers of 82% Au, and 4keV ions produced a 4nm layer of 43% Au. Such an effect would be barely observable in the RBS system used at McMaster, as described above.

Liau et al.[8] sputtered thin films of Cu_3Au on a Si substrate, with 40keV Ar^+ ions, at fluences between 5×10^{13} ions/mm^2 and 1.5×10^{15} ions/mm^2. They analysed

the effects by using 1.90 MeV He^+ ion RBS, tilting the target so that the He^+ beam was incident at 60^o to the surface normal. The result was that this geometry improved their depth resolution to about 10nm. They observed a surface layer with a composition of 27% Au, on a bulk of 25% Au. This small change is at the limit of the resolution of their RBS analysis system.

Färber et al.[25] sputtered bulk samples of Cu-Au alloys with 500eV and 1keV Ar^+ ions, at fluences up to 5×10^{15} ions/mm^2. They determined the composition of the surface 1nm-2nm by Auger electron spectroscopy (AES), and found no change in the relative heights of the AES signal peaks for Au and Cu. This contradicts Gillam's[24] results.

Figures 8 and 9 are typical of the results obtained in this work, for 45 keV Ar^+ ion sputtering. Figure 8 shows simple stoichiometric sputtering: $N_{Au}/N_{Cu} = S_{Au}/S_{Cu}$ = a constant to within 5%, the margin of error. In figure 9, the same is true, except that the initial sputtering rate is slower than the steady state rate. This is probably due to oxide and other contaminants on the surface, which reduce the sputtering yield of Cu and Au.

Figure 11 shows the steady-state total sputtering yields as a function of Cu in the Cu-Au films. These yields are somewhat lower than would be expected. Sigmund's

theory[1] gives: $S_{Au} \simeq 14$ atoms per ion for 30 keV Ar^+; $S_{Au} \simeq 15$ for 45 keV Ar^+; $S_{Cu} \simeq 6.8$ for 30 keV and 45 keV Ar^+. The published experimental data[26-30] exhibits some scatter, but all of these experiments show higher sputtering yields than observed in the Cu-Au alloy sputtering in this work, at McMaster. See Table IV and figure 11 for a comparison of results. The results seem to indicate that the Cu-Au films used in this work were slightly contaminated, probably with low atomic mass contaminants such as C and O, which would not be distinguishable in the RBS spectra unless present in large quantities. Andersen[26] has observed marked changes in the sputtering yield of Cu with small changes in impurity level.

Figure 12 shows the Ar^+ collection curves. There seems to be a general tendency to higher collection efficiency with increasing Cu content in the films. For the sample with 1% Cu, $\eta \simeq 4\%$; for the samples with about 70% Cu, $\eta \simeq 30\%$ at first, decreasing to about 10% after a fluence of about 3×10^{14} ions/mm^2 of 45 keV Ar^+; for the 94% Cu sample, $\eta \simeq 30\%$, decreasing slowly to about 20% after 5×10^{14} ions/mm^2 of 45 keV Ar^+.

Almén and Bruce[27] found that Cu implanted with 45 keV Ar^+ ions saturated at $N_T = 1.8 \times 10^{14}$ atoms/mm^2. In this work, the 94% Cu sample had not yet reached saturation at $N_T = 1.6 \times 10^{14}$ atoms/mm^2, but showed the beginnings of turnover. This may be due to three factors: a) the presence of 6% Au in the Cu may have created extra trapping

sites; b) the ion flux in this work was ~ 8 nA/mm^2, as compared to Almén and Bruce's[27] fluxes of 100 nA/mm^2 or greater - given more time to diffuse, the Ar atoms may have been trapped over a larger volume, allowing a greater number of atoms to be trapped; c) the contamination postulated to explain the sputtering yields may have created extra trapping sites.

Almén and Bruce[27] observed a saturation level of $N_T = 2.1 \times 10^{13}$ atoms/mm^2 for 45 keV Ar^+ ions implanted into Au. In this work, there was no sign of saturation of the Ar^+ in Au, at $N_T = 4.5 \times 10^{12}$ atoms/mm^2, when $I = 1.11 \times 10^{14}$ ions/mm^2. The data in figure 12 for 99% Au at $\Phi \approx 1.2 \times 10^{14}$ ions/mm^2 may be misleading, because by this time the 99% Au film had been sputtered until its thickness was less than twice the range of the 45 keV Ar^+ ions. Hence, a significant amount of Ar would be trapped in the SiO_2 substrate. It is strange that the collection curve should continue to be a straight line, with the same collection efficiency as the99% Au film, since they are such different kinds of materials.

Various researchers have observed the collection of Ar^+ ions implanted into Cu[31], Al[32], W[33], and glass[34], and Xe^+ ions implanted into Au[32], at low fluences, observing collection efficiencies of between 65% (30 kev Xe^+ into Au[32]) and nearly 100% (Ar^+ into Al[32]). They observed saturation at fluences of the order of 10^{12} ions/mm^2. The smallest

fluence used in this set of experiments was 1.4×10^{13} ions/mm^2. Therefore a 90% efficient collection mechanism which saturated at less than 10^{13} ions/mm^2 would not have been observed. The 4% — 30% collection efficiencies observed may have been due to secondary collection mechanisms, such as gas micro-bubble formation.

Almén and Bruce[27] observed that most elements reach saturation at values of N_T much greater than is the case for Cu and Au. They suggested that this might be due to greater thermal gas migration and out-diffusion. However, the experiment in this work with a 69% Cu, 31% Au film implanted at 50°K showed no greater trapping than the room temperature experiments, indicationg that thermal migration was not an important factor, unless the migrating species were mobile at 50°K, as is the case for some metal self-interstitials. Another possible explanation is that there was effective diffusion of the trapped atoms, caused by the mixing effect of the collision cascade resulting from the stopping of the energetic Ar^+ ions. Random walk theory says that, given a process in which an object moves a fixed distance X in a random direction, for each of N steps, then the average distance that object would move is $X\sqrt{N}$ from its starting position. At the turnover point in the 50°K collection curve, which is at $I \simeq 2 \times 10^{14}$ ions/mm^2, the Ar^+ ion cascades had displaced each target atom in the

region of the Ar^+ stopping approximately 50 times. The range of 45 keV Ar^+ in Cu is 13nm, and in Au is 11nm. If a displaced Ar atom recoils an average distance of $\sim$ 1nm before being stopped, (which is a reasonable estimate, based on Sigmund's[1] theory — see §2.1), then in 50 recoils, the average atom would move 1.0nm $\sqrt{50} \simeq$ 7nm from where it was originally trapped, given a random recoil process. Therefore a significant number of Ar atoms could have escaped by this "cascade mixing" process.

The other noticable feature of Fig. 9 is the second turnover point in the collection curves for the 71% Cu samples. The amount of Ar trapped seemed to have saturated, but then increased again, after the fourth He^+ ion beam analysis. At this point, the He^+ ions had displaced approximately one in six of the atoms in the target film. For sample #1, the turnover occurred after an implant of 3×10^{14} ions/mm^2 of Ar^+; in the region in which the Ar^+ ions were being slowed, the average target atom was displaced 80 times by the Ar^+ ions. This contrasts with the results for sample #2, in which the turnover point occurred after an implant of 6.7×10^{14} ions/mm^2 of Ar^+; here, the average number of displacements per atom was about 115, when account is taken for the sputter-removed atoms. The two samples in question were made in the same batch, and appeared to be identical, before being ion-irradiated.

A similar sample, with 69% Cu, was implanted at 50°K. Its collection curve did not show a second turnover. This may imply that the second turnover was due to a thermally dependent mechanism, related to the He^+ ion fluence.

One possible mechanism is void formation. He micro-voids might have been created by the agglomeration of several to several dozen implanted He atoms, once the concentration of He atoms and damage was high enough. These microvoids might then have acted as trapping sites for implanted Ar atoms. The agglomeration process could be thermally activated diffusion, in which case it would not occur at 50° K. Figures 10 a & b show scanning electron microscope photographs of the unirradiated and irradiated areas of the $Cu_{.71}Au_{.29}$ sample #2, showing small pits (~100nm in diameter) which could be Ar bubbles formed about He microvoids, exposed to the surface by sputtering. There is no literature on void formation by "low" fluence ($\sim 10^{16}/mm^2$) MeV He^+ ion implantation at room temperature, to support or contradict this idea. However, the range of MeV He^+ ions in metals is of the order of micrometers. The vast majority of the He^+ ions would pass right through the Cu-Au film, leaving a trail of damage. Another possible mechanism to describe the second turnover is that Ar atoms diffused thermally along the He^+ ion produced defects, to depths much greater than that of the Ar^+ ion produced

defects, once the defect concentration was high enough. Then the bubbles seen in figure 10b could be the result of the secondary collection mechanism postulated above.

Figures 10 and 11 show changes in the surface topography caused by the ion bombardment. Figure 10b is typical of the case of inert gas bubbles exposed by sputtering of the surface. Figures 11a and 11b show pyramid formation, similar to those formed in polycrystalline Cu targets [15, 16, 17]; although usually[15, 17] the structure is not as well developed at the relatively low fluence of 6.7×10^{14} ions/mm^2. This might indicate that the pyramids were Au, $CuAu_3$, CuAu, or Cu_3Au micro-crystals which were formed in the $Cu_{.94}Au_{.04}$ film under ion bombardment. The pyramids were too small to X-ray analyse in the S.E.M. system used, being only about 1μm across. The other samples did not show cone or pyramid formation.

CHAPTER 5

CONCLUSIONS

No preferential sputtering was observed when thin films of Cu-Au alloys were bombarded with 30 keV Ar^+, 45 keV Ar^+, and 45 keV Bi ions, to fluences of between 1.0×10^{13} ions/mm^2 and 8.3×10^{14} ions/mm^2. The depth resolution of the RBS system used was 17nm, therefore any changes of much less than 2% of the material in 17nm of film, i.e. $\lesssim 1.5 \times 10^{13}$ ions/mm^2, would not have been resolved. If there were a change in the composition of the surface 2nm, by as much as 15%, it would not have been observable.

The Ar collection efficiency in the films increased with increasing Cu content. The curves observed were probably due to secondary collection mechanisms, after a more efficient mechanism had already saturated, i.e., they were "quasi-saturation" curves. The anomalous second turnover in collection for the $Cu_{.71}Au_{.29}$ samples may have been due to Ar trapping at the He microvoid, or, more likely, to Ar diffusion via the He^+ ion produced defects, at greater depths than the Ar^+ ion produced defects.

The ion bombardment caused the formation of small (1μm) pyramids in $Cu_{.94}Au_{.06}$, but not in the other alloys.

These results are interesting, but it would require

considerable further experimentation to develop a good understanding of the processes involved.

TABLE I

Sputtering Yield Ratios for an Alloy $A_{.5}B_{.5}$; Low-Order Recoil Effect, Derived by Kelly[3], equation 8

M_A/M_B	S_A/S_B
0.143	7.0
0.333	3.2
1.00	1.0
3.00	0.31
7.00	0.14

TABLE II

Sputtering Yield Ratios for an Alloy $A_{.5}B_{.5}$; Cascade Effect, Derived by Haff[4], equation 10

M_A/M_B	S_A/S_B
0.143	1.63
0.333	1.32
1.00	1.00
3.00	0.76
7.00	0.61

TABLE III

Sputtering Yield Ratios for an Alloy $A_{.5}B_{.5}$; Surface Binding Energy Effect, Derived by Kelly[3], equation 18

System	S_A/S_B
Ag-Au	1.15
Ag-Mg	0.73
Ag-Pd	1.15
Al-Au	1.08
Au-Cu	0.94
Cu-Ni	1.13
Fe-Ni	1.04

TABLE IV

Theoretical and Experimental Sputtering Yields

Target	Ar^+ Energy	S (atoms/ion)	Reference
Cu	30 keV	6.8	1
		6.0	27
		8.5	29
Cu	45keV	6.8	1
		9.0	26
		6.8	27
		8.5	29
Au	30 keV	14	1
		9.0	30
Au	45 keV	15	1
		10.2	27
		9.0	30
Cu_3Au	40 keV	7.1	8
$Cu_{.75}Au_{.25}$	30 keV	4.8	
$Cu_{.94}Au_{.06}$		3.7	
$Cu_{.71}Au_{.29}$		4.9, 6.0	this work
$Cu_{.69}Au_{.31}$	45 keV	4.4 (@50°K)	(McMaster)
$Cu_{.01}Au_{.99}$		6.9	

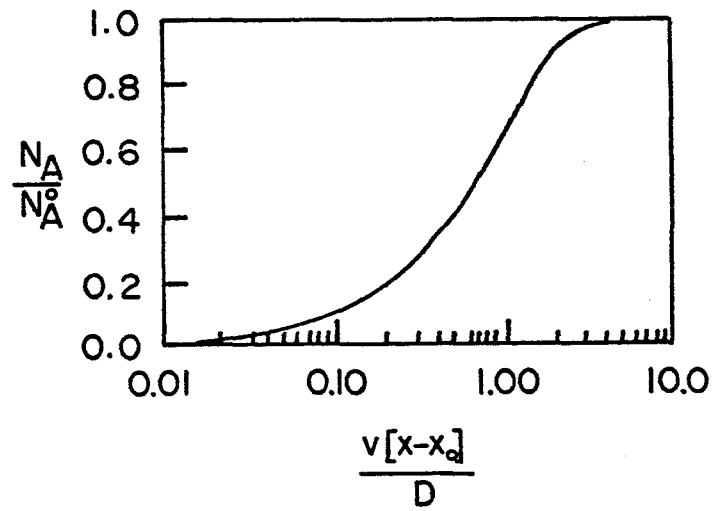

Figure 1: Pickering Model: Steady-State Concentration Profile of Component A

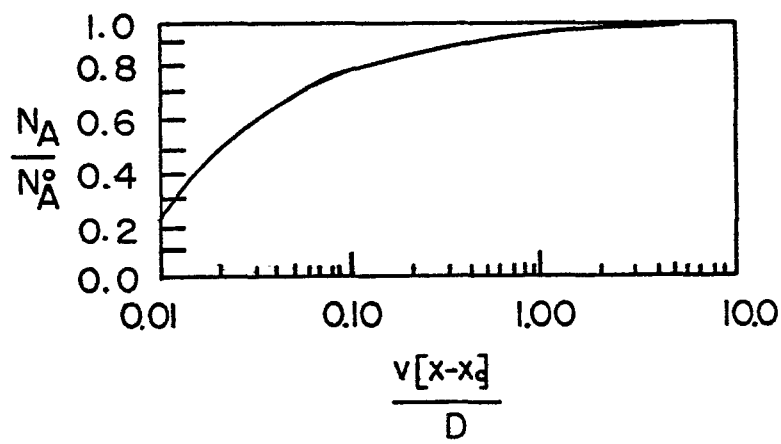

Figure 2: Collins Model: Steady Concentration Profile of Component A

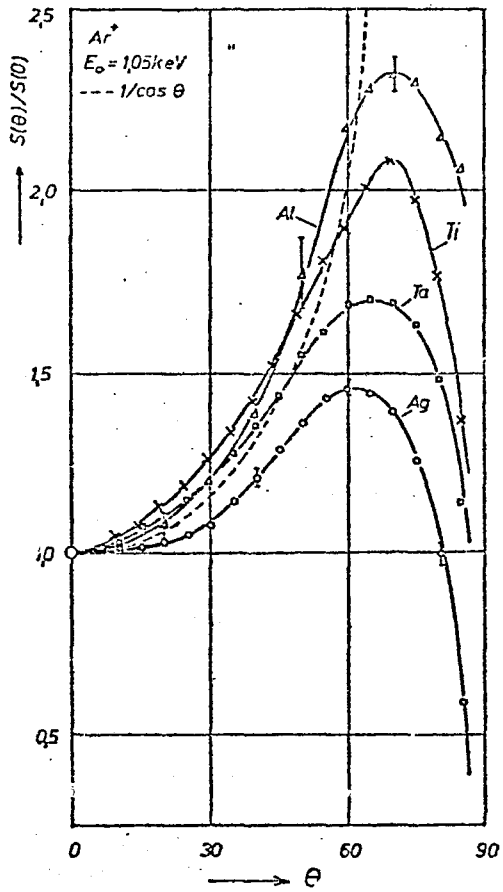

Figure 3: Variation of Sputtering Yield with Ion Incidence Angle

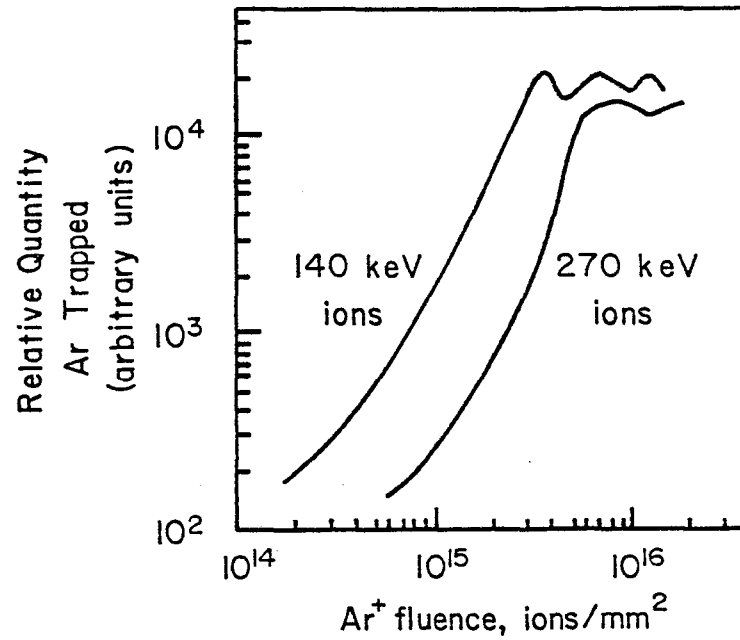

Figure 4: Non-Monotonic Collection of Ar in Si

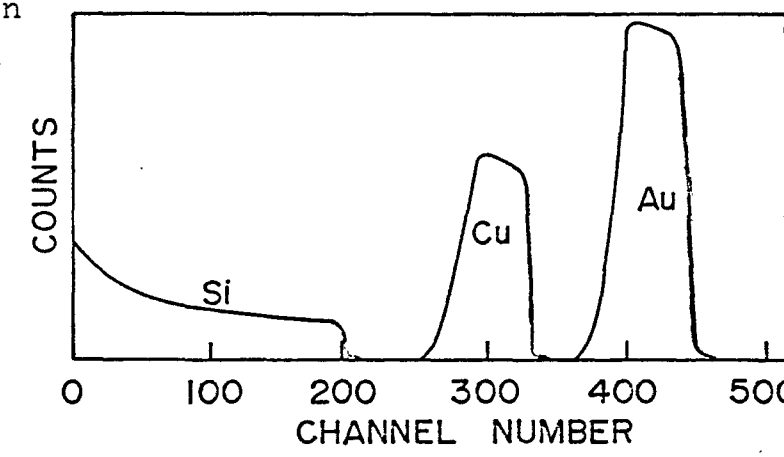

Figure 5: RBS Spectrum of $Cu_{.71}Au_{.29}$ on Si Substrate; 2.0 MeV He^+, $\theta_L = 150^\circ$

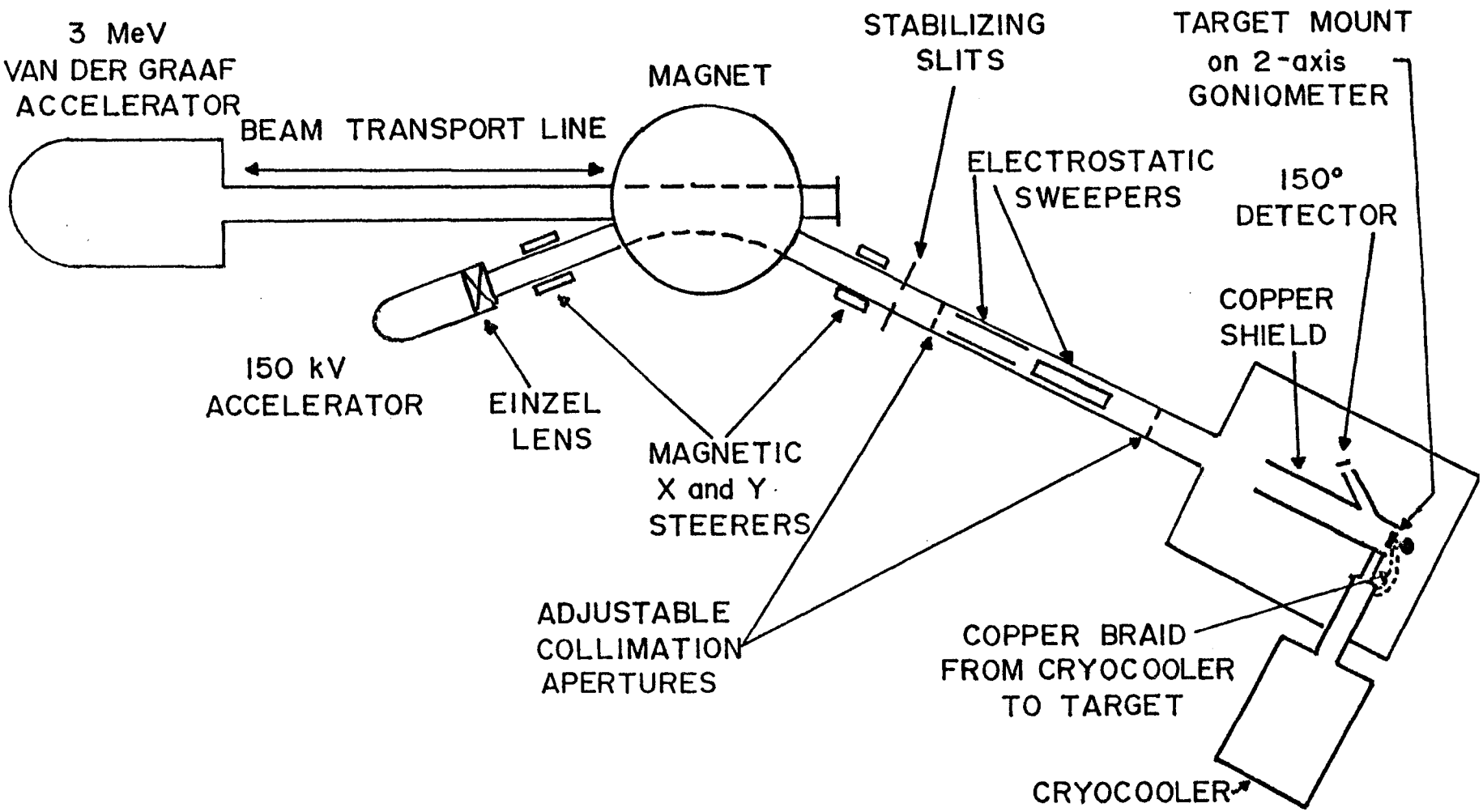

Figure 6: Schematic of McMaster On-Line RBS and Ion Implantation Facility

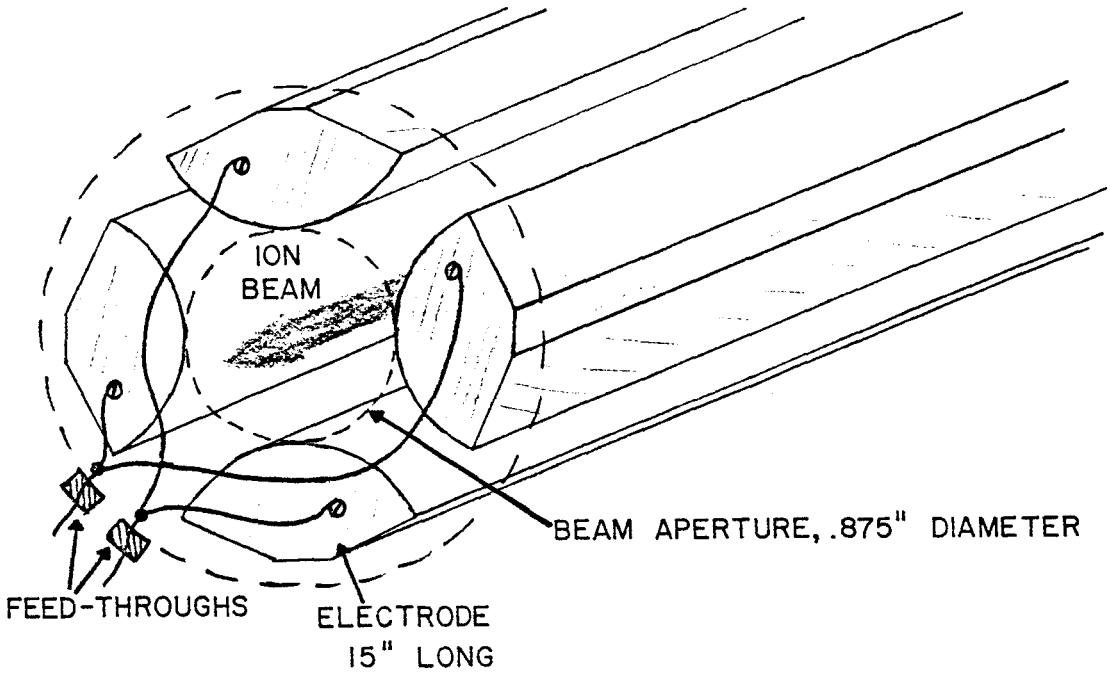

Figure 7: Schematic of Electrostatic Quadrupole

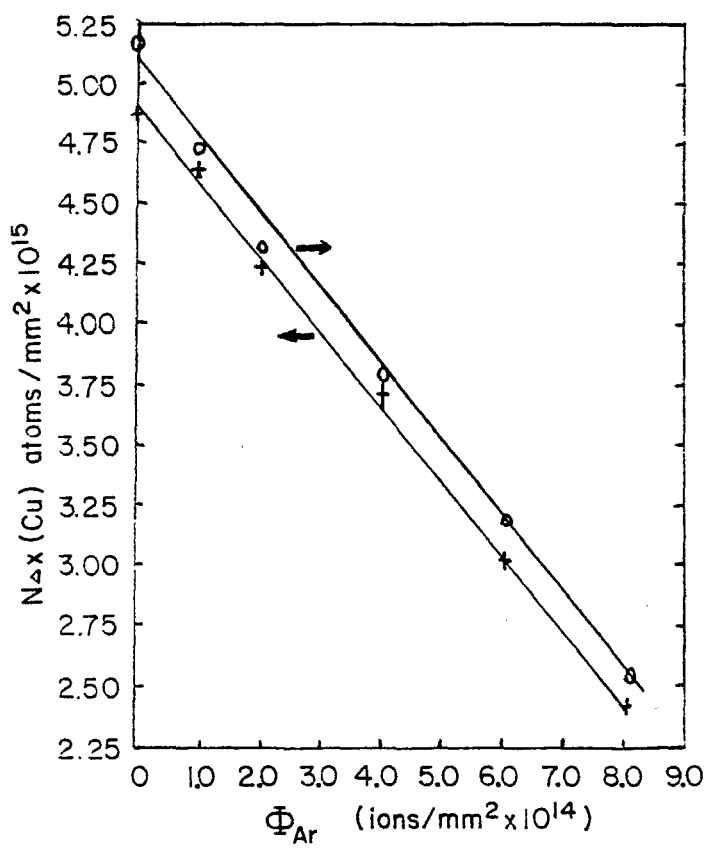

Figure 8: Sputtering of $Cu_{.69}Au_{.31}$ by 45 keV Ar^+

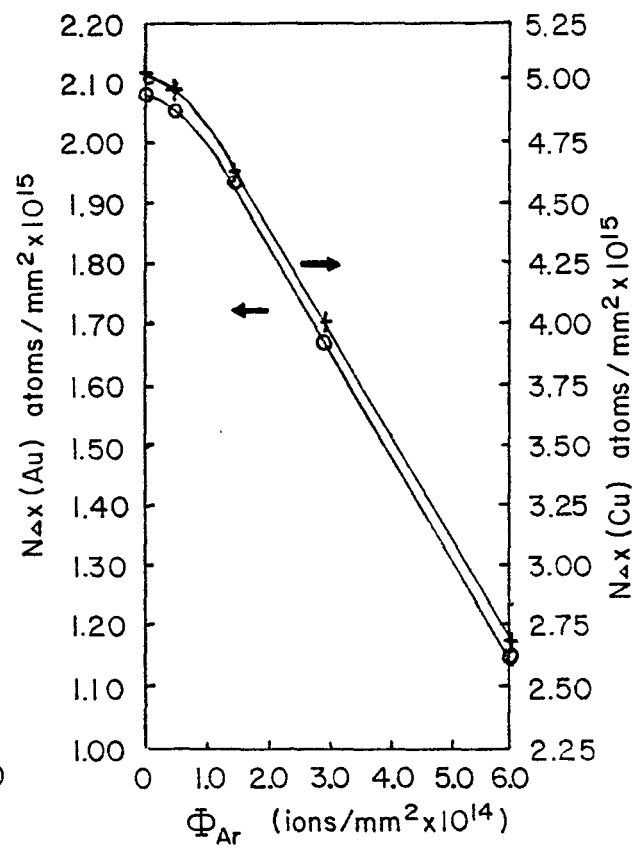

Figure 9: Sputtering of $Cu_{.71}Au_{.29}$ (sample #1) by 45 keV Ar^+

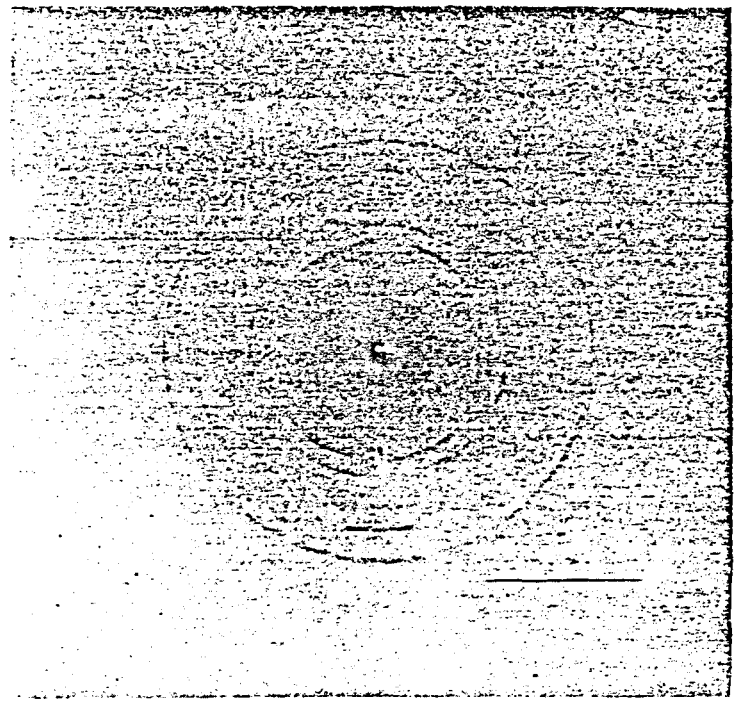

Figure 10a: before ion bombardment

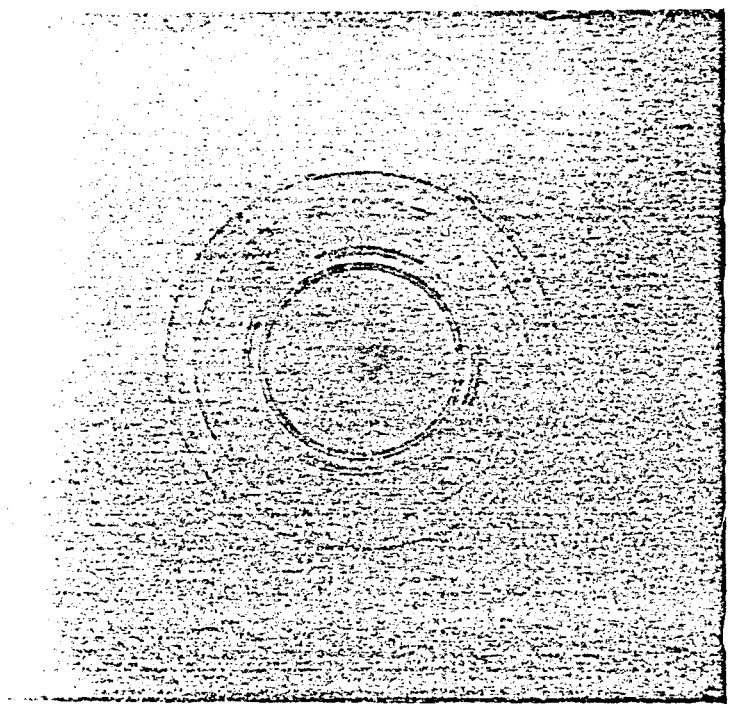

Figure 10b: after bombardment with 500 eV Ar^+

Figure 10: T.E.M. Electron Diffraction Patterns of Cu_3Au

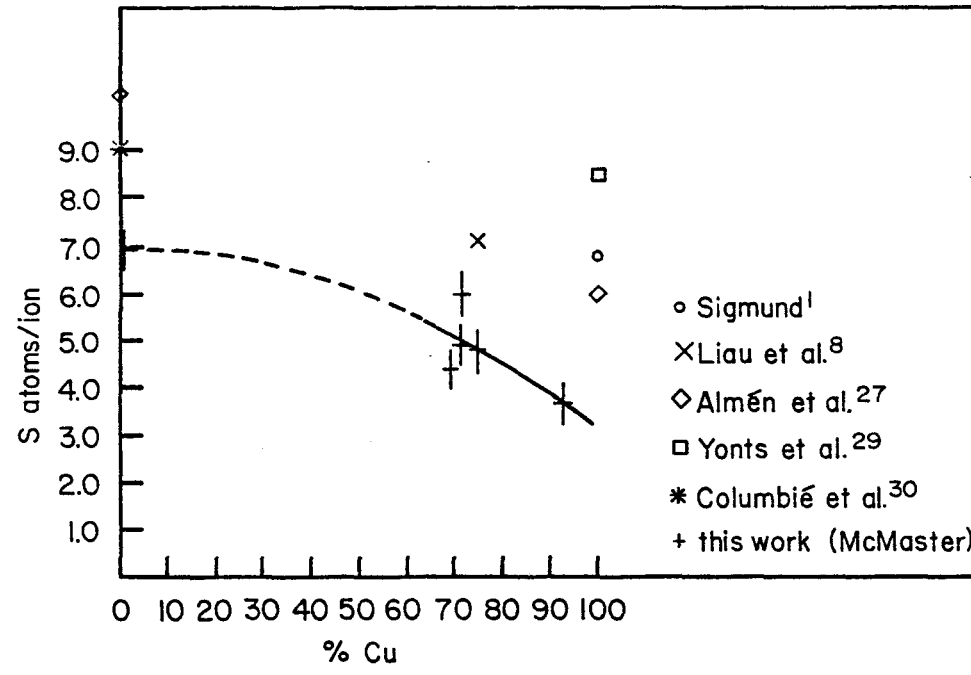

Figure 11: Sputtering of Cu-Au alloy Films with 30 and 45 keV Ar^+

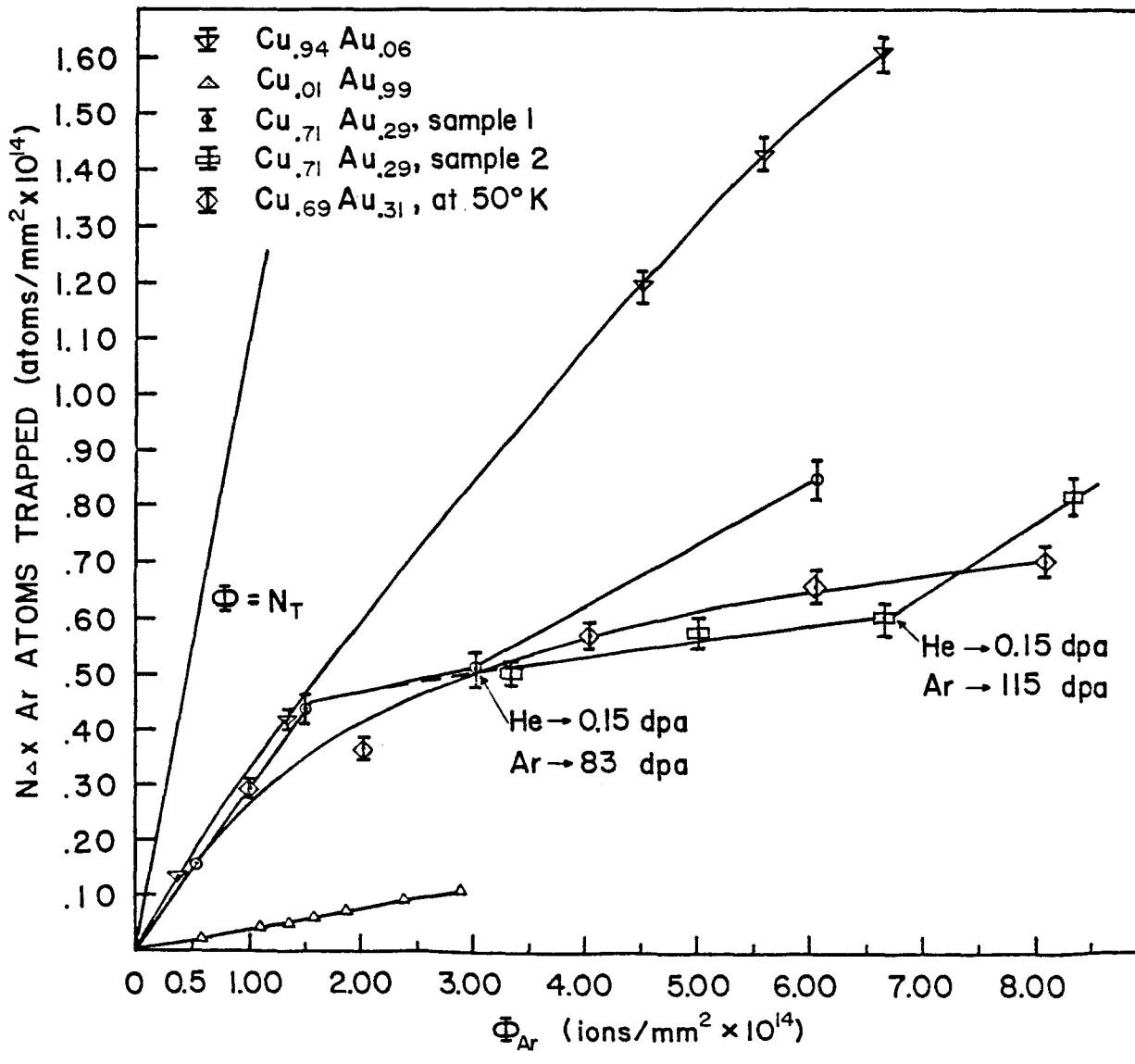

Figure 12: 45 keV Ar^+ Collection Curves in Cu-Au Alloy Films

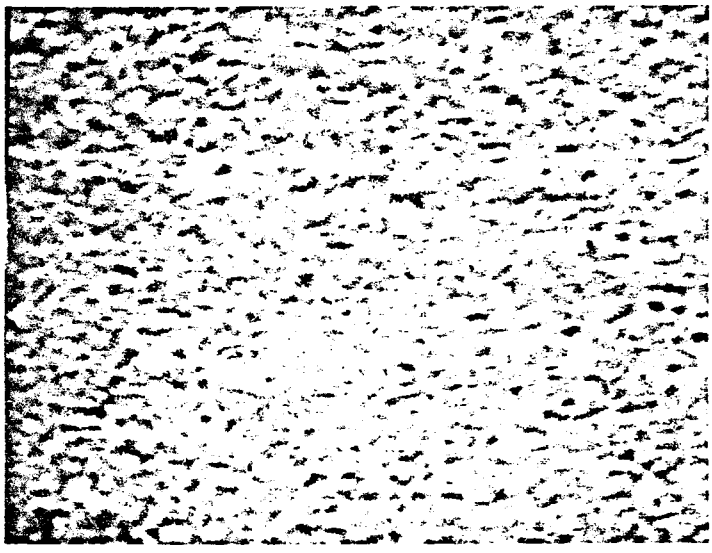

Figure 13a: before ion bombardment

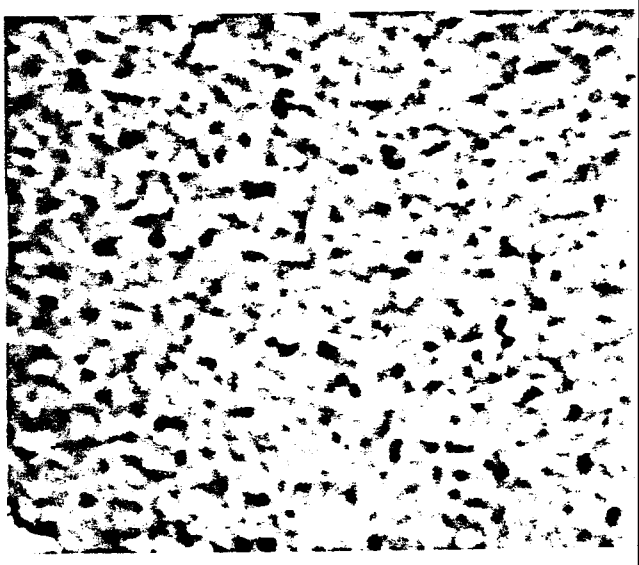

Figure 13b: after bombardment with 8.3×10^{14} ions/mm^2 of 45 keV Ar^+

Figure 13: S.E.M. Photographs of $Cu_{.71}Au_{.29}$ (sample #2)

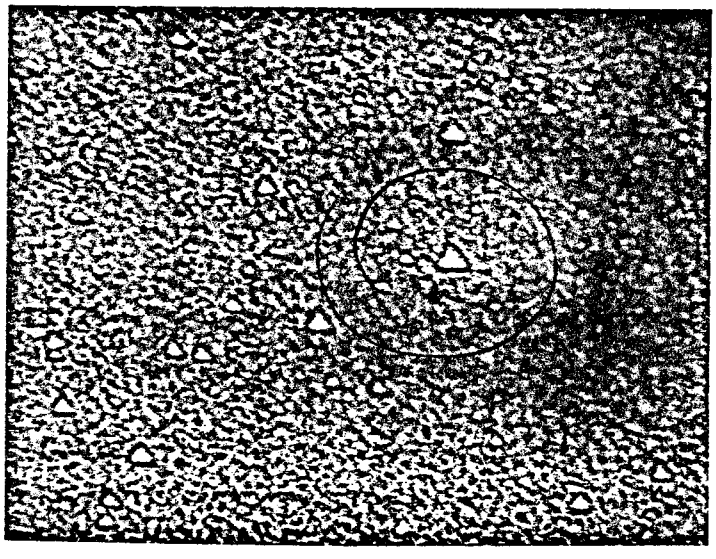

Figure 14a: 5,000X magnification

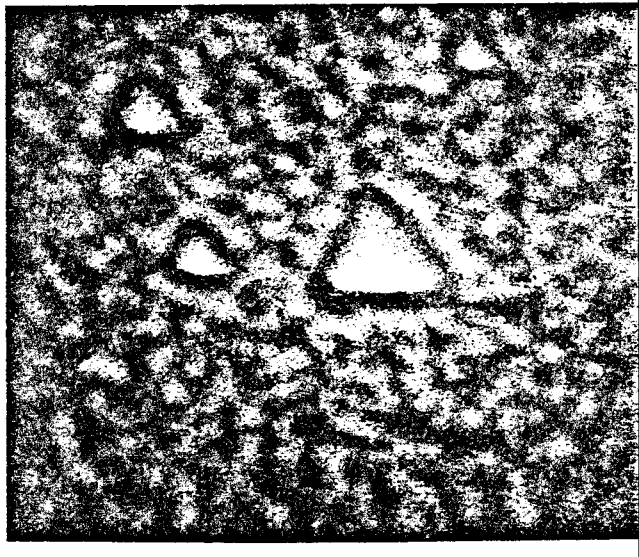

Figure 14b: 20,000X magnification

Figure 14: S.E.M. Photographs of $Cu_{.94}Au_{.06}$ after 6.7×10^{14} ions/mm^2 of 45 keV Ar^+

REFERENCES

1) P. Sigmund, Phys. Rev. 184 (1969) 396

2) D.A. Thompson, J. Appl. Phys, to be published

3) R. Kelly, Nucl. Instr. and Meth. 149 (1978) 553

4) R. Kelly, J.B. Sanders, Surf. Sci. 57 (1976) 143

5) P.K. Haff, Appl. Phys. Lett. 31 (1977) 259

6) H.F. Winters, P. Sigmund, J. Appl. Phys. 45 (1974) 4760

7) N. Andersen, P. Sigmund, Proc. Int. Conf. on At. Coll. in Solids, Plenum Press, N.Y. 1975, Vol. 1, 115

8) Z.L. Liau, W.L. Brown, R. Homer, J.M. Poate, Appl. Phys. Lett. 30 (1977) 626

9) H. Shimizu, M. Ono, K. Nakayama, Surf. Sci. 36 (1973) 817

10) H.W. Pickering, J. Vac. Sci. Tech., Vol. 13 #2 (1976) 618

11) R. Collins, Rad. Eff. 37 (1978) 13

12) R. Webb, G. Carter, R. Collins, Rad. Eff. 39 (1978) 129

13) H. Oechsner, Appl. Phys. 8 (1975)

14) J.L.Whitton, G. Carter, M. Nobes, J.S. Williams, Rad. Eff. 32 (1977) 129

15) G. Carter, J.S. Colligon, M. Nobes, Rad. Eff. 31 (1977) 65

16) G.W. Lewis, J.S. Colligon, F. Paton, M. Nobes, G. Carter, J.L. Whitton, Rad. Eff. Lett. 43 (1979) 49

17) O. Auciello, R. Kelly, R. Iricibar, Rad. Eff. Lett. 43 (1979) 37

18) G. Carter, D.G. Armour, S.E. Donnelly, D.C. Ingram, R. Webb, Proc. Harwell Conf., Sept. 1979

19) K. Wittmaack, P. Blank, W. Wach, Rad. Eff. 39 (1978) 81

20) P. Blank, K. Wittmaack, Rad. Eff. Lett. 43 (1979) 105

21) J.L. Ecuyer, M. Matsunami, J.A. Davies, Nucl. Instr. and Meth. 160 (2); (1979) 337

22) P. Townsend, J.C. Kelly, N.E.W. Hartley, "Ion Impl., Sputt. and their Appl." Academic Press, (1976) 181

23) P.W. Hawkes, "Quadrupoles in Electrostatic Lenses", Academic Press, N.Y., 1970

24) E. Gillam, J. Phys. Chem. Sol. 11 (1959) 55

25) W. Färber, G. Betz, P. Braun, Nucl. Instr. and Meth. 132 (1976) 351

26) H. Andersen, H. Bay, Rad. Eff. 13 (1972) 67

27) O. Almén, G. Bruce, Nucl. Instr. and Meth. 11 (1961) 257

28) O. Almén, G. Bruce, Nucl. Instr. and Meth. 11 (1961) 279

29) O.C. Yonts, C.E. Normand, D.E. Harrison, J. Appl. Phys. 31 (1960) 447

30) N. Colombié, thesis, University of Toulouse, 1964

31) A. Cavaleru, C.M. Morley, D.G. Armour, G. Carter, Rad. Eff. 18 (1973) 87

32) F. Brown, J.A. Davies, Can. J. Phys. 41 (1963) 844

33) E.V. Kornelsen, Can. J. Phys. 42 (1964) 364

34) A. Cavaleru, D.G. Armour, G. Carter, Vacuum 22 (1972) 321